Letter-of-Intent to PAC46

Physics with Positron Beams at Jefferson Lab 12 GeV

John Arrington[1], Marco Battaglieri[2], Jan Bernauer[3], Angela Biselli[10], M Bondí, Volker Burkert[4], Lucien Causse[5], Andrea Celentano[2], Pierre Chatagnon[5], Maxime Defurne[6], Raphaël Dupré[5], Mathieu Ehrhart[5], Latifa Elouadrhiri[4], Frédéric Georges[4], François-Xavier Girod[4], Joseph Grames[4], Michel Guidal[5], Ho-San Ko[5], Dominique Marchand[5], Luca Marsicano[2,7], Carlos Muñoz Camacho[5], M De Napoli, Silvia Niccolai[5], Axel Schmidt[3], Daria Sokhan[8], Mike Tiefenback[4], Paolo Valente[9], Raffaella De Vita[2], Eric Voutier[5], Rong Wang[5], Shenying Zhao[5]

[1] *Argonne National Laboratory*
9700 S. Cass Avenue, Argonne, Illinois 60439, USA

[2] *Istituto Nazionale di Fisica Nucleare*
Sezione di Genova
Via Dodecaneso, 33 - 16146 Genova, Italia

[3] *Laboratory for Nuclear Science*
Massachusetts Institute of Technology
77 Massachusetts Avenue, Cambridge, Massachusetts 02139, USA

[4] *Thomas Jefferson National Accelerator Facility*
12000 Jefferson Avenue, Newport News, Virginia 23606, USA

[5] *Institut de Physique Nucléaire*
Université Paris-Sud & Paris-Saclay
15 rue Georges Clémenceau, 91406 Orsay cedex, France

[6] *Institut de Recherche sur les Lois Fondamentales de l'Univers*
Commissariat à l'Energie Atomique, Université Paris-Saclay
91191 Gif-sur-Yvette, France

[7] *Universita' Di Genova*
Via Balbi, 5 - 16126 Genova, Italia

[8] *University of Glasgow*

University Avenue, Glasgow G12 8QQ, United Kingdom

[9] *Istituto Nazionale di Fisica Nucleare*
Sezione di Roma
Piazzale Aldo Moro, 2 - 00185 Roma, Italia

[10] *Fairfield University*
1073 N Benson Road, Fairfield, Connecticut 06824, USA

Letter-of-Intent as of 23 May 2018

Contact persons: grames@jlab.org, voutier@ipno.in2p3.fr

Abstract

Table of contents

1 Introduction

Quantum Electrodynamics (QED) is one of the most powerful quantum physics theories. The highly accurate predictive power of this theory allows not only to investigate numerous physics phenomena at the macroscopic, atomic, nuclear, and partonic scales, but also to test the validity of the Standard Model. Therefore, QED promotes electrons and positrons as unique physics probes, as demonstrated worldwide over decades of scientific research at different laboratories.

Both from the projectile and target point of views, spin appears nowadays as the finest tool for the study of the intimate structure of matter. Recent examples from the experimental physics program developed at the Thomas Jefferson National Accelerator Facility (JLab) include: the measurement of polarization observables in elastic electron scattering off the nucleon [Jon00, Gay02, Puc10], that established the unexpected magnitude and behaviour of the proton electric form factor at high momentum transfer (see [Pun15] for a review); the experimental evidence, in the production of real photons from a polarized electron beam interacting with unpolarized protons, of a strong sensitivity to the orientation of the longitudinal polarization of the electron beam [Ste01], that opened the investigation of the 3-dimensional partonic structure of nucleons and nuclei via the generalized parton distributions [Mul94] measured through the deeply virtual Compton scattering [Ji97, Rad97]; the achievement of a unique parity violation experimental program [Arm05, Ani06, And13] accessing the smallest ever measured polarized beam asymmetries ($\sim 10^{-7}$), which provided the first determination of the weak charge of the proton [And13] and allowed for stringent tests of the Standard Model at the TeV mass-scale [You06]; etc. Undoubtably, polarization became an important capability and a mandatory property of the current and next accelerator generation.

The combination of the QED predictive power and the fineness of the spin probe led to a large but yet limited variety of impressive physics results. Adding to this tool-kit charge symmetry properties in terms of polarized positron beams will provide a more complete and accurate picture of the physics at play, independently of the size of the scale involved. In the context of the experimental study of the structure of hadronic matter worked-out at JLab, the electromagnetic interaction dominates lepton-hadron reactions and there is no stringent difference between the physics information obtained from the scattering of electrons or positrons off an hadronic target. However, every time a reaction process is a conspiracy of more than one elementary mechanism, the comparison between electron and positron scatterings allows us to isolate the quantum interference between these mechanisms. This is of particular interest for studying limitations of the one-photon exchange Born approximation in elastic and inelastic scatterings [Gui03]. It is also essential for the experimental determination of the generalized parton distributions where the interference between the known Bethe-Heitler process and the unknown deeply virtual Compton scattering requires polarized and unpolarized electron and positron beams for a model independent extraction [Vou14]. Such polarized lepton beams also provide the ability to test the existence of a new physics beyond the frontiers of the Standard Model. ... More text about C_{3q}

(?) and dark matter search.

The production of high-quality polarized positron beams relevant to these many applications remains however a highly difficult task that, until recently, was feasible only at large scale accelerator facilities. Relying on the most recent advances in high polarization and high intensity electron sources [Add10], the PEPPo (Polarized Electrons for Polarized Positrons) technique [Abb16], demonstrated at the injector of the Continuous Electron Beam Accelerator Facility (CEBAF), provides a novel and widely accessible approach based on the production, within a tungsten target, of polarized e^+e^- pairs from the circularly polarized bremsstrahlung radiation of a low energy highly polarized electron beam. As opposed to other schemes operating at GeV lepton beam energies [Sok64, Omo06, Ale08], the operation of the PEPPo technique requires only energies above the pair-production threshold and is teherefore ideally suited for a polarized positron beam at CEBAF.

This document...

2 Physics motivations

2.1 Elastic lepton scattering

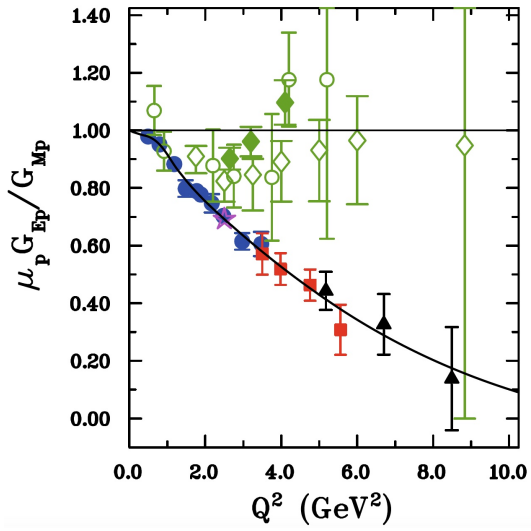

Figure 1. Rosenbluth (green symbols) and polarization transfer (blue, red, and black symbols) experimental data about the ratio between the electric and magnetic form factor of the proton, together with an empirical fit of polarization data [Pun15].

The measurement of the electric form factor of the nucleon (G_E) at high momentum transfer, in the perspective of the experimental assessment of perturbative Quantum Chromo-Dynamics (QCD) scaling laws [Bro81], motivated an intense experimental effort targeted by the advent of high energy continuous polarized electron beams. Indeed, the polarization observables technique [Akh74, Arn81] is expected to be more sensitive to G_E than the cross sec-

tion method relying on a Rosenbluth separation [Ros50]. However, the strong disagreement between the results of these two experimental methods (Fig. 1) came as a real surprise. Following the very first measurements of polarization transfer observables in the $^1\mathrm{H}(\vec{e}, e\vec{p})$ reaction [Jon00], the validity of the Born approximation for the description of the elastic scattering of electrons off protons was questionned. The eventual importance of higher orders in the α-development of the electromagnetic interaction was suggested [Gui03] as an hypothesis to reconciliate cross section and polarization transfer experimental data, while making impossible a model-independent experimental determination of the nucleon electromagnetic form factors via solely electron scattering.

Considering the possible existence of second order contributions to the electromagnetic current, the so-called 2γ-exchange, the eN-interaction is no longer characterized by 2 real form factors but by 3 generalized complex form factors

$$\widetilde{G}_M = e\, G_M + \delta\widetilde{G}_M\,, \quad \widetilde{G}_E = e\, G_E + \delta\widetilde{G}_E\,, \quad \widetilde{F}_3 = \delta\widetilde{F}_3\,, \tag{1}$$

where e represents the lepton beam charge. These expressions involve up to 8 unknown real quantities that should be recovered from experiments [Rek04]. Considering unpolarized leptons, the non point-like structure of the nucleon can be expressed by the reduced cross section

$$\begin{aligned}\sigma_R^e = \tau G_M^2 + \epsilon G_E^2 + 2e\,\tau G_M\, \Re e\left[\delta\widetilde{G}_M\right] \\ + 2e\,\epsilon\, G_E\, \Re e\left[\delta\widetilde{G}_E\right] + e\,\sqrt{\tau(1-\epsilon^2)(1+\tau)}G_M\, \Re e\left[\delta\widetilde{F}_3\right]\end{aligned} \tag{2}$$

where the charge dependent contributions denote the additional contributions from the 2γ-exchange mechanisms. The variable ϵ characterizing, in the 1γ-exchange approximation, the virtual photon polarization writes

$$\epsilon = \left[1 - 2\frac{\vec{q}\cdot\vec{q}}{Q^2}\tan^2\left(\frac{\theta_e}{2}\right)\right]^{-1} \tag{3}$$

where θ_e is the electron scattering angle, $q \equiv (\vec{q}, \omega)$ is the virtual photon with four-mometum transfer $Q^2{=}{-}q\cdot q$, and $\tau{=}Q^2/4M^2$ with M representing the nucleon mass. In absence of lepton beams of opposite charge, the Rosenbluth method, consisting in the measurement of the reduced cross section at different ϵ-values while keeping constant Q^2, allows the determination of a combination of 1γ and 2γ electromagnetic form factors and requires consequently some model-dependent input to separate further the electric and magnetic form factors.
The transfer of the longitudinal polarization of a lepton beam via the elastic scattering off a nucleon provides 2 additionnal and different linear combinations of the same physics quantities in the form of the transverse (P_t^e) and longitudinal (P_l^e) polarization components of the nucleon

$$\sigma_R^e\, P_t^e = -\,\lambda\sqrt{2\epsilon\tau(1-\epsilon)}\,\Bigg(\; G_E G_M + e\, G_E \Re e\left[\delta\widetilde{G}_M\right] \tag{4}$$
$$+\, e\, G_M \Re e\left[\delta\widetilde{G}_E\right] + e\sqrt{\frac{1+\epsilon}{1-\epsilon}} G_E \Re e\left[\delta\widetilde{F}_3\right]\Bigg)$$
$$\sigma_R^e P_l^e = \lambda\,\tau\sqrt{1-\epsilon^2}\Bigg(G_M^2 + e\,\left[2+\sqrt{\frac{1+\tau}{\tau(1-\epsilon)}}\right] G_M \Re e\left[\delta\widetilde{F}_3\right]\Bigg). \tag{5}$$

where λ is the lepton beam polarization. The combination of polarized and unpolarized beam observables of elastic electron scattering involve up to 6 unknown real quantities, requiring at least 6 independent experimental observables. Therefore, taking into account 2γ-exchange mechanisms electron beams only can no longer provide an experimental alone determination of the electromagnetic form factors of the nucleon. However, comparing polarized electron and positron beams, one can separate the charge dependent and independent contributions of experimental observables i.e. separate the 1γ and 2γ form factors. For instance,

$$\frac{\sigma_R^+ + \sigma_R^-}{2} = \tau G_M^2 + \epsilon G_E^2 \tag{6}$$
$$\frac{\sigma_R^+ - \sigma_R^-}{2} = 2\tau G_M\, \Re e\left[\delta\widetilde{G}_M\right] \tag{7}$$
$$+\, 2\,\epsilon\, G_E\, \Re e\left[\delta\widetilde{G}_E\right] + \sqrt{\tau(1-\epsilon^2)(1+\tau)} G_M\, \Re e\left[\delta\widetilde{F}_3\right]$$

and similarly for polarized observables. Consequently, the measurement of polarized and unpolarized elastic scattering of both electrons and positrons provide the necessary data for a model independent determination of the nucleon electromagnetic form factors.

2.2 Deep inelastic lepton scattering

The understanding of the partonic structure and dynamics of hadronic matter is the major goal of modern Nuclear Physics. The availability of high intensity continuous polarized electron beams with high energy together with performant detector systems at different facilities is providing today an unprecedented but still limited insight into this problem. Similarly to the elastic scattering case, the combination of measurements with polarized electrons and polarized positrons in the deep inelastic regime will allow to obtain unique experimental observables enabling a strict model-independent interpretation.

The generalized parton distribution (GPD) framework [Mul94] constitutes the most appealling and advanced parameterization of the hadron structure. It encodes the intimate structure of matter in terms of quarks and gluons and unifies within the same framework electromagnetic form factors, parton distributions, and the description of the nucleon spin (see [Die03, Bel05] for a review). GPDs can be interpreted as the probability to find at a given trans-

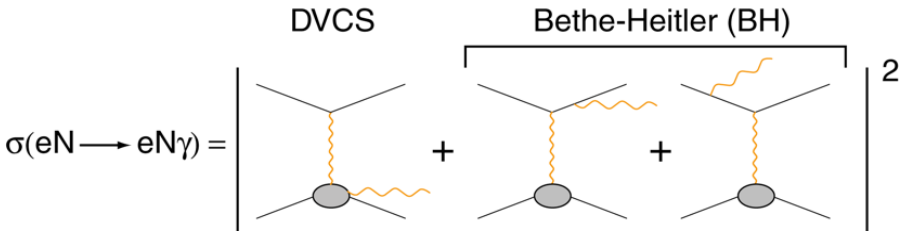

Figure 2. Lowest order QED amplitude of the electroproduction of real photons off nucleons(nuclei).

verse position a parton carrying a certain fraction of the longitudinal momentum of the nucleon. The combination of longitudinal and transverse degrees of freedom is responsible for the richness of this universal framework.

GPDs are involved in any deep process and are preferentially accessed in hard lepto-production of real photons i.e. deeply virtual Compton scattering (DVCS). This process competes with the known Bethe-Heitler (BH) reaction [Bet34] where real photons are emitted from initial or final leptons instead of the probed hadronic state (Fig. 2). The lepton beam charge and polarization dependence of the $eN(A)\gamma$ cross section off nucleons(nuclei) writes [Die09]

$$\sigma^{e}_{\lambda 0} = \sigma_{BH} + \sigma_{DVCS} + \lambda\,\widetilde{\sigma}_{DVCS} + e\,\sigma_{INT} + e\lambda\,\widetilde{\sigma}_{INT} \tag{8}$$

where the index INT denotes the interference contribution to the cross section originating from the quantum interference of the BH and DVCS processes. Polarized electron scattering provide the experimental observables

$$\sigma^{-}_{00} = \frac{\sigma^{-}_{+0} + \sigma^{-}_{-0}}{2} = \sigma_{BH} + \sigma_{DVCS} - \sigma_{INT}\,, \tag{9}$$

$$^{1}\Delta^{-}_{\lambda 0} = \frac{\sigma^{-}_{+0} - \sigma^{-}_{-0}}{2} = \lambda\,[\widetilde{\sigma}_{DVCS} - \widetilde{\sigma}_{INT}] \tag{10}$$

involving unseparated combinations of the unknwon INT and $DVCS$ reaction amplitudes. The comparison between polarized electron and polarized positron reactions provides the additional observables

$$\Delta\sigma_{00} = \frac{\sigma^{+}_{00} - \sigma^{-}_{00}}{2} = \sigma_{INT} \tag{11}$$

$$^{2}\Delta_{\lambda 0} = \frac{^{1}\Delta^{+}_{\lambda 0} - {}^{1}\Delta^{-}_{\lambda 0}}{2} = \lambda\,\widetilde{\sigma}_{INT} \tag{12}$$

which isolate the interference amplitude. Consequently, measuring real photon lepto-production off nucleons(nuclei) with opposite charge polarized leptons allows to separate the four unknown contributions to the $eN(A)\gamma$ cross section.
For a spin s hadron, one can define $(2s+1)^2$ parton helicity conserving and chiral even elementary GPDs that can be accessed through DVCS. They appear within the reaction amplitudes in the form of unseparated linear and bi-linear

expresssion. Their separation requires additional observables that can be obtained considering polarized targets (S) [Bel02]. The full lepton beam charge and polarizations dependence of the $eN(A)\gamma$ cross section can be written generically [Die09]

$$\begin{aligned}\sigma^{e}_{\lambda S} &= \sigma^{e}_{\lambda 0} \\ &+ S\left[\lambda\,\Delta\sigma_{BH} + \lambda\,\Delta\sigma_{DVCS} + \Delta\widetilde{\sigma}_{DVCS} + e\lambda\,\Delta\sigma_{INT} + e\,\Delta\widetilde{\sigma}_{INT}\right].\end{aligned} \tag{13}$$

where $\Delta\sigma_{BH}$ is the known sensitivity of the BH process to the target polarization and the remaining terms feature four new combinations of the nucleon GPDs to be isolated. Polarized electron scattering provides the combinations

$${}^{1}\Delta\sigma^{-}_{0S} = \frac{\sigma^{-}_{0+} - \sigma^{-}_{0-}}{2} = S\,\left[\Delta\widetilde{\sigma}_{DVCS} - \Delta\widetilde{\sigma}_{INT}\right] \tag{14}$$

$${}^{2}\Delta^{-}_{\lambda S} = \frac{{}^{1}\Delta^{-}_{\lambda +} - {}^{1}\Delta^{-}_{\lambda -}}{2} = S\,\lambda\,\left[\Delta\sigma_{BH} + \Delta\sigma_{DVCS} - \Delta\sigma_{INT}\right] \tag{15}$$

and the comparison between polarized electrons and positrons yields

$${}^{2}\Delta\sigma_{0S} = \frac{{}^{1}\Delta\sigma^{+}_{0S} - {}^{1}\Delta\sigma^{-}_{0S}}{2} = S\,\Delta\widetilde{\sigma}_{INT} \tag{16}$$

$${}^{3}\Delta_{\lambda S} = \frac{{}^{2}\Delta^{+}_{\lambda S} - {}^{2}\Delta^{-}_{\lambda S}}{2} = S\,\lambda\,\Delta\sigma_{INT} \tag{17}$$

which once again isolates the interference contribution and allows to separate the four reaction amplitudes of interest.
Polarized positron beams then appear as a mandatory complement to polarized electron beams for a model independent determination of nucleons and nuclei GPDs.

2.3 Test of the Standard Model

3 Polarized positron beam at CEBAF

4 TPE-CLAS12

Spokesperons:

5 TPE-SBS

Spokesperons:

6 pDVCS-CLAS12

Spokesperons:

7 n-DVCS @ CLAS12

Beam Charge Asymmetries for Deeply Virtual Compton Scattering on the Neutron with CLAS12 at 11 GeV

Abstract

Measuring DVCS on a neutron target is a necessary step to deepen our understanding of the structure of the nucleon in terms of GPDs. The combination of neutron and proton targets allows to perform a flavor decomposition of the GPDs. Moreover, DVCS on a neutron target plays a complementary role to DVCS on a transversely polarized proton target in the determination of the GPD E, the least known and constrained GPD that enters Ji's angular momentum sum rule. We propose to measure, for the first time, the beam charge asymmetry (BCA) in the $e^{\pm}d \to e^{\pm}n\gamma(p)$ reactions, with the upgraded 11 GeV CEBAF positron/electron beams and the CLAS12 detector. The exclusivity of the final state will be ensured by detecting in CLAS12 the scattered lepton, the photon (including the Forward Tagger at low polar angles), and the neutron. Running 80 days on a deuterium target at the maximum CLAS12 luminosity (10^{35} cm^{-2}·s^{-1}) will yield a rich BCA data set in the 4-dimensional (Q^2, x_B, $-t$, ϕ) phase space. This observable will significantly impact the experimental determination of the real parts of the $\mathcal{E}_n$ and, to a lesser extent, $\widetilde{\mathcal{H}_n}$ Compton form factors.

Spokespersons: S. Niccolai (niccolai@ipno.in2p3.fr), E. Voutier

It is well known that the fundamental particles which form hadronic matter are the quarks and the gluons, whose interactions are described by the QCD Lagrangian. However, exact QCD-based calculations cannot yet be performed to explain all the properties of hadrons in terms of their constituents. Phenomenological functions need to be used to connect experimental observables with the inner dynamics of the constituents of the nucleon, the partons. Typical examples of such functions include form factors, parton densities, and distribution amplitudes. The GPDs are nowadays the object of intense research effort in the perspective of unraveling nucleon structure. They describe the correlations between the longitudinal momentum and transverse spatial position of the partons inside the nucleon, they give access to the contribution of the orbital momentum of the quarks to the nucleon, and they are sensitive to the correlated $q\bar{q}$ components of the nucleon wave function [Mul94, Die03, Bel05].

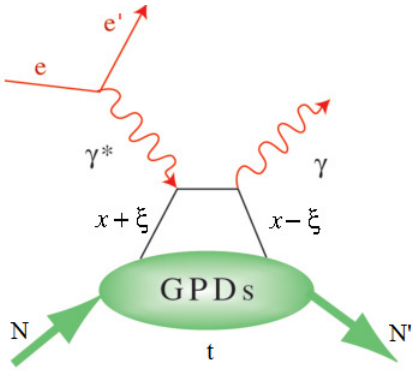

Figure 3. The handbag diagram for the DVCS process on the nucleon $eN \to e'N'\gamma'$; here $x+\xi$ and $x-\xi$ are the longitudinal momentum fractions of the struck quark before and after scattering, respectively, and $t = (N - N')^2$ is the squared four-momentum transfer between the initial and final nucleons. $\xi \simeq x_B/(2 - x_B)$ is proportional to the Bjorken scaling variable $x_B = Q^2/2M\nu$, where M is the nucleon mass and ν is the energy transfer to the quark.

The nucleon GPDs are the structure functions which are accessed in the measurement of the exclusive leptoproduction of a photon (DVCS) or of a meson on the nucleon, at sufficiently large photon virtuality (Q^2) for the reaction to happen at the parton level. Figure 3 illustrates the leading process for DVCS, also called "handbag diagram". At leading-order QCD and at leading twist, considering only quark-helicity conserving quantities and the quark sector, the process is described by four GPDs: $H^q, \widetilde{H^q}, E^q, \widetilde{E^q}$, one for each quark flavor q, that account for the possible combinations of relative orientations of the nucleon spin and quark helicities between the initial and final states. H^q and E^q do not depend on the quark helicity and are therefore called unpolarized GPDs while $\widetilde{H^q}$ and $\widetilde{E^q}$ depend on the quark helicity and are called polarized GPDs. H^q and $\widetilde{H^q}$ conserve the spin of the nucleon, whereas E^q and $\widetilde{E^q}$ correspond to a nucleon-spin flip.
The GPDs depend upon three variables, x, ξ and t: $x + \xi$ and $x - \xi$ are the longitudinal momentum fractions of the struck quark before and after scattering, respectively, and t is the squared four-momentum transfer between

the initial and final nucleon (see caption of Fig. 3 for definitions). The transverse component of t is the Fourier-conjugate of the transverse position of the struck parton in the nucleon. Among these three variables, only ξ and t are experimentally accessible with DVCS.

The DVCS amplitude is proportional to combinations of integrals over x of the form

$$\int_{-1}^{1} dx\, F(\mp x, \xi, t) \left[\frac{1}{x - \xi + i\epsilon} \pm \frac{1}{x + \xi - i\epsilon} \right], \tag{18}$$

where F represents one of the four GPDs. The top combination of the plus and minus signs applies to unpolarized GPDs (H^q, E^q), and the bottom combination of signs applies to the polarized GPDs ($\widetilde{H^q}, \widetilde{E^q}$). Each of these 4 integrals or Compton Form Factors (CFFs) can be decomposed into their real and imaginary parts, as following:

$$\Re\mathrm{e}\left[\mathcal{F}(\xi,t)\right] = \mathcal{P}\int_{-1}^{1} dx \left[\frac{1}{x-\xi} \mp \frac{1}{x+\xi} \right] F(x,\xi,t) \tag{19}$$

$$\Im\mathrm{m}\left[\mathcal{F}(\xi,t)\right] = -\pi[F(\xi,\xi,t) \mp F(-\xi,\xi,t)], \tag{20}$$

where $\mathcal{P}$ is Cauchy's principal value integral and the sign convention is the same as in Eq. 18. The information that can be extracted from the experimental data at a given (ξ, t) point depends on the measured observable. $\Re\mathrm{e}[\mathcal{F}]$ is accessed primarily measuring observables which are sensitive to the real part of the DVCS amplitude, such as double-spin asymmetries, beam charge asymmetries or unpolarized cross sections. $\Im\mathrm{m}[\mathcal{F}]$ can be obtained measuring observables sensitive to the imaginary part of the DVCS amplitude, such as single-spin asymmetries or the difference of polarized cross-sections. However, knowing the CFFs does not define the GPDs uniquely. A model input is necessary to deconvolute their x-dependence.
The DVCS process is accompanied by the BH process (Fig. 2), in which the final-state real photon is radiated by the incoming or scattered electron and not by the nucleon itself. The BH process, which is not sensitive to GPDs, is experimentally indistinguishable from DVCS and interferes with it at the amplitude level (Sec. 2.2). However, considering that the nucleon form factors are well known at small t, the BH process is precisely calculable.

7.2 Neutron GPDs and flavor separation

The importance of neutron targets in the DVCS phenomenology was clearly established in the pioneering Hall A experiment, where the polarized-beam cross section difference off a neutron, from a deuterium target, was measured [Maz07]. Measuring neutron GPDs in complement to proton GPDs allows for a quark-flavor separation. For instance, the $\mathcal{E}$-CFF of the proton and the neutron can be expressed as

$$\mathcal{E}_p(\xi,t) = \frac{4}{9}\mathcal{E}^u(\xi,t) + \frac{1}{9}\mathcal{E}^d(\xi,t) \tag{21}$$

$$\mathcal{E}_n(\xi,t) = \frac{1}{9}\mathcal{E}^u(\xi,t) + \frac{4}{9}\mathcal{E}^d(\xi,t) \tag{22}$$

(and similarly for $\mathcal{H}$, $\widetilde{\mathcal{H}}$ and $\widetilde{\mathcal{E}}$). It follows that

$$\mathcal{E}^u(\xi,t) = \frac{9}{15}\left[4\mathcal{E}_p(\xi,t) - \mathcal{E}_n(\xi,t)\right] \tag{23}$$

$$\mathcal{E}^d(\xi,t) = \frac{9}{15}\left[4\mathcal{E}_n(\xi,t) - \mathcal{E}_p(\xi,t)\right] . \tag{24}$$

An extensive experimental program dedicated to the measurement of the DVCS reaction on a proton target has been approved at Jefferson Lab, in particular with CLAS12. Single-spin asymmetries with polarized beam and/or linearly or transversely polarized proton targets, as well as unpolarized and polarized cross sections, will be measured with high precision over a vast kinematic coverage. A similar experimental program on the neutron will make possible the flavor separation of the various GPDs. The beam spin asymmetry for n-DVCS, particularly sensitive to the GPD E_n will be soon measured at CLAS12, using an experimental technique different from the initial Hall A measurement and involving the neutron detection [Nic11]. Additionnally, the measurement of single- and double-spin asymmetries with a longitudinally polarized neutron target is also foreseen for the nearby future at CLAS12 [Nic15]. The present LOI focuses on the extraction of one more observable, the beam charge asymmetry. The next sections outline the benefits of this observable for the CFFs determination.

7.3 Beam charge asymmetry

Considering unpolarized electron and positron beams, the sensitivity of the cross-section to the lepton beam charge (Sec. 2.2) can be expressed with the beam charge asymmetry observable [Hos16]

$$A_{\rm C}(\phi) = \frac{d^4\sigma^+ - d^4\sigma^-}{d^4\sigma^+ + d^4\sigma^-} = \frac{d^4\sigma^{\rm I}_{UU}}{d^4\sigma^{\rm BH}_{UU} + d^4\sigma^{\rm DVCS}_{UU}} \tag{25}$$

which isolates the BH-DVCS interference contribution at the numerator and the DVCS amplitude at the denominator. Following the harmonic decomposition of observables proposed in Ref. [Bel02],

$$d^4\sigma^{\rm BH}_{UU} = \frac{K_1}{\mathcal{P}_1(\phi)\,\mathcal{P}_2(\phi)} \sum_{n=1}^{2} c^{\rm BH}_{n,\rm unp}\cos(n\phi) \tag{26}$$

$$d^4\sigma^{\rm DVCS}_{UU} = \frac{K_3}{Q^2} \sum_{n=0}^{2} c^{\rm DVCS}_{n,\rm unp}\cos(n\phi)\,, \tag{27}$$

and

$$d^4\sigma^{\rm I}_{UU} = \frac{K_2}{\mathcal{P}_1(\phi)\,\mathcal{P}_2(\phi)} \sum_{n=0}^{3} c^{\rm I}_{n,\rm unp} \cos(n\phi) \tag{28}$$

where K_i's are kinematical factors, and $P_i(\phi)$'s are the BH propagators. Because of the $1/Q^2$ kinematical suppression of the DVCS amplitude, the dominant contribution to the denominator originates from the BH amplitude. This approximation depends on the kinematics and, in the most general case, the DVCS contribution in the denominator only complicates the extraction of CFFs. At leading twist, the dominant coefficients to the numerator are $c^{\rm I}_{0,\rm unp}$ and $c^{\rm I}_{1,\rm unp}$

$$c^{\rm I}_{0,\rm unp} \propto -\frac{\sqrt{-t}}{Q}\, c^{\rm I}_{1,\rm unp} \tag{29}$$

$$c^{\rm I}_{1,\rm unp} \propto \Re{\rm e}\left[F_1\mathcal{H} + \xi(F_1+F_2)\widetilde{\mathcal{H}} - \frac{t}{4M^2}F_2\mathcal{E}\right]. \tag{30}$$

Given the relative strength of F_1 and F_2 at small t for a neutron target, the beam charge asymmetry becomes

$$A_{\rm C}(\phi) \propto \frac{1}{F_2}\,\Re{\rm e}\left[\xi\widetilde{\mathcal{H}_n} - \frac{t}{4M^2}\mathcal{E}_n\right]. \tag{31}$$

Therefore, the BCA is mainly sensitive to the real part of the GPD E_n and, for selected kinematics, to the real part of the GPD $\widetilde{H_n}$.

Considering polarized electron and positron beams, two additional observables can be constructed in the form of the charge difference ($\Delta^{LU}_{\rm C}$) and charge average ($\Sigma^{LU}_{\rm C}$) beam helicity asymmetries [Hos16]

$$\Delta^{LU}_{\rm C}(\phi) = \frac{(d^4\sigma^+_+ - d^4\sigma^+_-) - (d^4\sigma^-_+ - d^4\sigma^-_-)}{d^4\sigma^+_+ + d^4\sigma^+_- + d^4\sigma^-_+ + d^4\sigma^-_-} = \frac{d^4\sigma^{\rm I}_{LU}}{d^4\sigma^{\rm BH}_{UU} + d^4\sigma^{\rm DVCS}_{UU}} \tag{32}$$

$$\Sigma^{LU}_{\rm C}(\phi) = \frac{(d^4\sigma^+_+ - d^4\sigma^+_-) + (d^4\sigma^-_+ - d^4\sigma^-_-)}{d^4\sigma^+_+ + d^4\sigma^+_- + d^4\sigma^-_+ + d^4\sigma^-_-} = \frac{d^4\sigma^{\rm DVCS}_{LU}}{d^4\sigma^{\rm BH}_{UU} + d^4\sigma^{\rm DVCS}_{UU}} \tag{33}$$

which singles out in two separate observables the beam polarization sensitivity of the interference and DVCS amplitudes. Following Ref. [Bel02], these write

$$d^4\sigma^{\rm I}_{LU} = \frac{K_2}{\mathcal{P}_1(\phi)\,\mathcal{P}_2(\phi)} \sum_{n=1}^{2} s^{\rm I}_{n,\rm unp} \sin(n\phi) \tag{34}$$

$$d^4\sigma^{\rm DVCS}_{LU} = \frac{K_3}{Q^2}\, s^{\rm DVCS}_{1,\rm unp} \sin(\phi) \tag{35}$$

where $s^{\rm I}_{1,\rm unp}$ is the dominant twist-2 contribution, proportional to the imaginary part of $c^{\rm I}_{1,\rm unp}$ (Eq. 30); $s^{\rm I}_{2,\rm unp}$ and $s^{\rm DVCS}_{1,\rm unp}$ are twist-3 contributions with distinct GPD dependence and different harmonic behaviour.

... text continues...

7.4 Projected data

We are proposing to measure the beam charge asymmetry for the electroproduction of photons on a neutron using a liquid deuterium target, the 11 GeV CEBAF electron beam, and the proposed 11 GeV positron beam. The scattered electrons and photons will be detected with the CLAS12 detector in its baseline configuration, completed at small angles with the forward electromagnetic calorimeter of the Forward Tagger (FT). The detection of the struck neutrons will be accomplished with the CND (Central Neutron Detector) and the CTOF (Central Time-of-Flight) at backwards angles, and the FEC (Forward Electromagnetic Calorimeter), the PCAL (Preshower Calorimeter), and the FTOF (Forward Time-of-Flight) at forward angles. In order to match the detector acceptance for the different lepton beam charges, the positron data taking will be performed with opposite polarities for the CLAS12 torus and solenoid, with respect to the electron data taking.

An event generator (GENEPI) for the DVCS, the BH and exclusive π^0 electroproduction processes on the neutron inside a deuterium target was developed [Ala09]. The DVCS amplitude is calculated according to the BKM formalism [Bel02], while the GPDs are taken from the standard CLAS DVCS generator [Van99, Goe01]. The initial Fermi-motion distribution of the neutron is determined from the Paris potential [Lac80]. The output of the event generator was fed through CLAS12 FASTMC, to simulate acceptance and resolution effects on electrons/positrons and photons in the Forward Detector (FD). For the detection of photons with polar angles between 2.5^o and 4.5^o the Forward Tagger (FT) will be used [Bat11]. Kinematic cuts to ensure the applicability of the GPD formalism ($Q^2 > 1$ GeV$^2/c^2$, $t > -1.2$ GeV$^2/c^2$, $W > 2$ GeV) have been applied. Figure 4(left) shows the coverage in Q^2, x_B and t obtained for the D$(e, en\gamma)p$ reaction with an electron or positron beam energy of 11 GeV and the appropriate magnet polarities. The three plots in Fig. 4(right) shows the energy/momentum distributions of final state particles: as expected,the scattered leptons and the photons are mostly emitted at forward angles, while the recoil neutrons populate dominantly the backward angles region. The CND and the CTOF will detect the large angle neutrons with a global efficiency ∼10-12%, while the remaining neutrons will be detected in the forward scintillator-based detectors of CLAS12 (FEC, FTOF, PCAL).

The expected number of reconstructed $en\gamma(p)$ events has been determined as a function of the kinematics. An overall 10% neutron-detection efficiency for neutrons with $\theta > 40^o$ has been assumed. The detection efficiencies for electrons/positrons and photons are assumed to be 100%, within the fiducial cuts. Considering the always-improving performance of the CLAS12 data acquisition system, the operation of CLAS12 at its design luminosity $\mathcal{L} = 10^{35}$ cm^{-2}·s^{-1} per nucleon, corresponding to 60 nA electron and positron beam currents, is assumed for the present data projections. An overall data taking time of 80 days, equally shared between electrons and positrons, is also con-

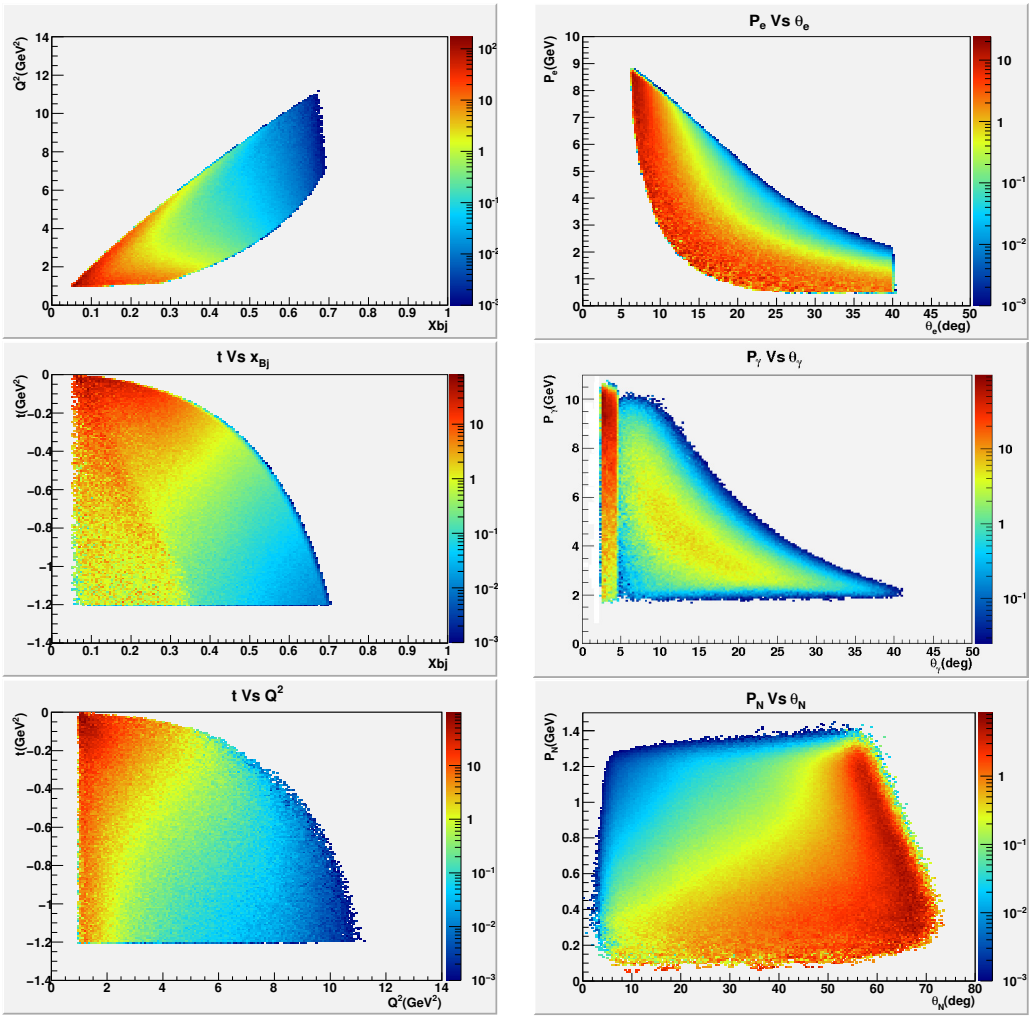

Figure 4. (left) Distributions of the kinematic variables for n-DVCS events, including acceptance and physics cuts: (Q^2, x_B) phase space (top), (t, x_B) phase space (middle), and (t, Q^2) phase space (bottom). (right) Momentum distribution as function of polar angle for the $en\gamma(p)$ final state: electron/positron (top), photon (middle), and neutron momentum (bottom).

sidered. The following 4-dimensional grid of bins has been adopted:

- 4 bins in Q^2 $[1, 2, 3.5, 5, 10$ GeV$^2/c^2]$;
- 4 bins in $-t$ $[0, 0.2, 0.5, 0.8, 1.2$ GeV$^2/c^2]$;
- 4 bins in x_B $[0.05, 0.15, 0.3, 0.45, 0.7]$;
- 12 bins in ϕ, each 30^o wide.

For each bin, the beam charge asymmetry (BCA) is experimentally reconstructed following

$$A_{\rm C} = \frac{(N^+/Q^+) - (N^-/Q^-)}{(N^+/Q^+) - (N^-/Q^-)} \tag{36}$$

where $Q^{\pm}$ is the integrated charge for lepton beam of each polarity (Q^+=Q^- in the present evaluation), and $N^{\pm}$ is the corresponding number of $en\gamma(p)$

events. For each bin $N^{\pm}$ is computed as:

$$N^{\pm} = \mathcal{L}^{\pm} \cdot \Delta T \cdot \frac{d\sigma}{dQ^2 dx_B dt d\phi} \cdot \Delta t \cdot \Delta Q^2 \cdot \Delta x_B \cdot \Delta\phi \cdot \mathcal{A} \cdot \epsilon_n \qquad (37)$$

where $\mathcal{L}^{\pm}$ is the beam luminosity, ΔT is the running time, $d^4\sigma/dQ^2 dx_B dt d\phi$ is the 4-fold differential cross section, $\Delta Q^2 \Delta x_B \Delta t \Delta\phi$ is the full bin width, $\mathcal{A}$ is the bin-to-bin acceptance, and ϵ_n is the neutron-detection efficiency. The statistical errors on the BCA depend on the BCA magnitude through the formula:

$$\sigma\left(A_{\mathrm{C}}\right) = \sqrt{\frac{1 - A_{\mathrm{C}}^2}{N}} \qquad (38)$$

where $N{=}N^{+}{+}N^{-}$ is the total number of events. Figure 5 shows the expected statistical accuracy of the planned BCA measurements, where the BCA magnitude is obtained at each bin from the VGG model assuming $J_u = 0.3$ and $J_d = 0.1$. Summing $N^{\pm}$ over for the full grid of bins, an overall $25{\times}10^6$ $en\gamma(p)$ events are expected to be collected over the full kinematic range of interest for 80 days of running.

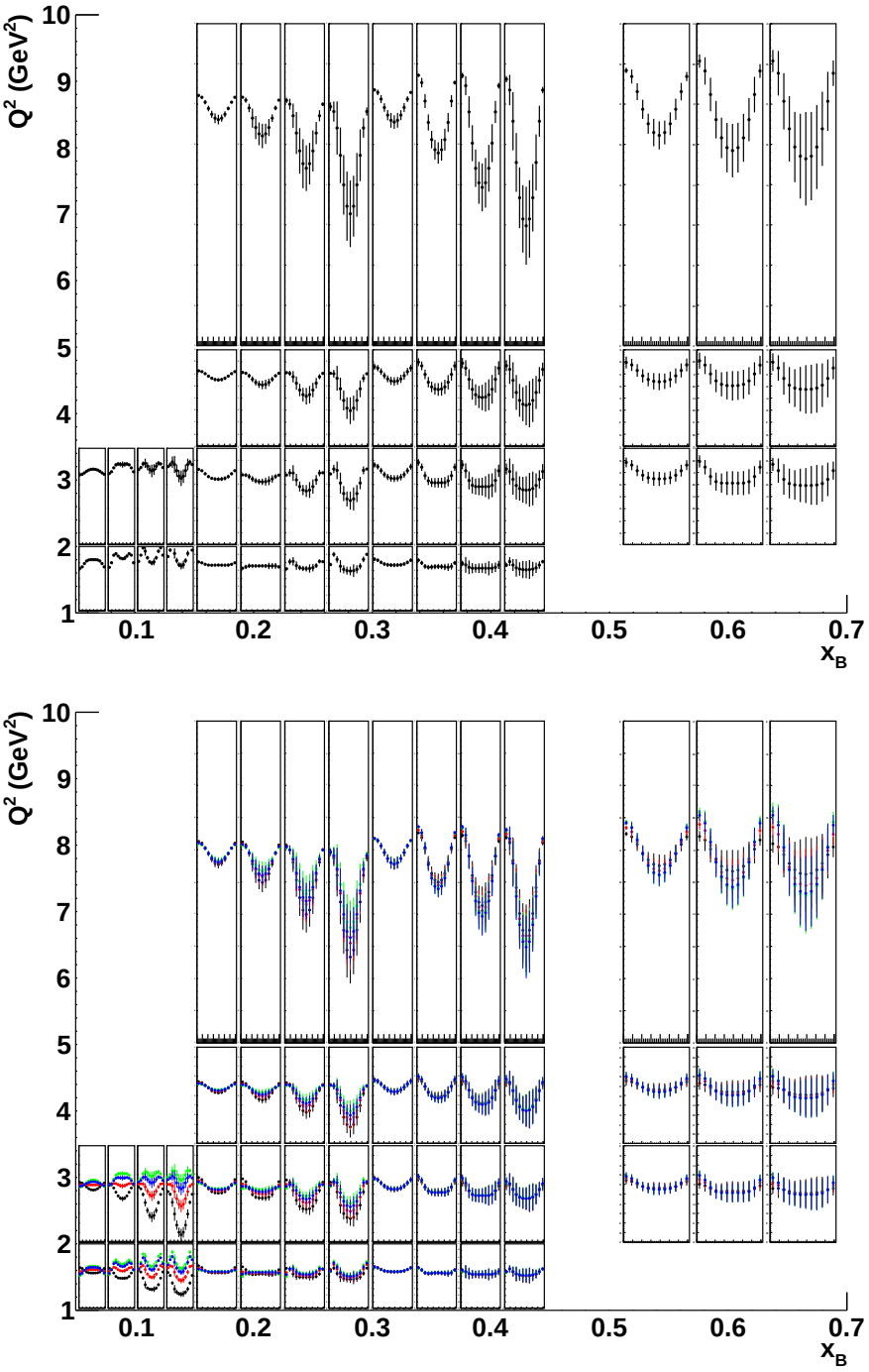

Figure 5. Projected BCA data for the D$(e, en\gamma)p$ reaction as predicted by the VGG model for $(J_u, J_d) = (0.3, 0.1)$ (top) and alternative combinations (bottom). The bottom plot compares (J_u, J_d): $(0.3, 0.1)$ (black), $(0.2, 0.0)$ (red), $(0.1,\text{-}0.1)$ (green), and $(0.3,\text{-}0.1)$ (blue). The vertical axis scale ranges from -0.3 to 0.1 for the top plot and from -0.3 to 0.2 for the bottom plot. The error bars reflect the expected statistical uncertainties for 80 days of beam time at a luminosity of 10^{35} cm^{-2}·s^{-1} per nucleon.

7.5 Extraction of Compton form factors

In order to establish the impact of proposed experiment on the CLAS12 n-DVCS program, the four sets of projected asymmetries BSA [Nic11]), TSA and DSA [Nic15], and BCA (Fig. 5), for all kinematic bins, were processed using a fitting procedure [Gui08, Gui13] to extract the neutron CFFs. This approach is based on a local-fitting method at each given experimental $(Q^2, x_B, -t)$ kinematic point. In this framework, there are eight real CFF-related quantities

$$F_{Re}(\xi,t) = \Re\mathrm{e}\left[\mathcal{F}(\xi,t)\right] \tag{39}$$

$$F_{Im}(\xi,t) = -\frac{1}{\pi}\Im\mathrm{m}\left[\mathcal{F}(\xi,t)\right] = \left[F(\xi,\xi,t) \mp F(-\xi,\xi,t)\right], \tag{40}$$

where the sign convention is the same as for Eq. 18. These CFFs are the almost-free [1] parameters to be extracted from DVCS observables using the well-established theoretical description of the process based on the DVCS and BH mechanisms. The BH amplitude is calculated exactly while the DVCS one is determined at the QCD leading twist [Van99].

As there are eight CFF-related free parameters, including more observables measured at the same kinematic points will result in tighter constraint on the fit and will increase the number and accuracy of extracted CFFs. In the adopted version of the fitter code, $\widetilde{E_{Im}}(n)$ is set to zero, as $\widetilde{E_n}$ is assumed to be purely real. Thus, seven out of the eight real and imaginary parts of the CFFs are left as free parameters in the fit. The results for the 7 neutron CFFs are shown in Figs. 6-11, as a function of $-t$, and for each bin in Q^2 and x_B. The blue points are the CFFs resulting from the fits of the four observables, while the red ones are the CFFs obtained fitting only the projections of the currently approved n-DVCS experiments. The error bars reflect both the statistical precision of the fitted observables and their sensitivity to that particular CFFs. Only results for which the error bars are non zero, and therefore the fits properly converged, are included in the figures.
The major impact of the proposed experiment is, as expected, on $E_{Re}(n)$, for which the already approved projections have hardly any sensitivity. Thanks to the proposed BCA data $E_{Re}(n)$ will be extracted over basically the whole phase. A considerable extension in the coverage will be also obtained for $\widetilde{H_{Re}}(n)$. An overall improvement to the precision on the other CFFs, as well as an extension in their kinematic coverage will also be induced by the proposed n-DVCS BCA dataset.

7.6 Systematic uncertainties

The goal of this experiment is to measure beam charge asymmetries which are ratios of absolute cross sections. In this ratio, several charge-independent

[1] The values of the CFFs are allowed to vary within ±5 times the values predicted by the VGG model [Van99, Gui05].

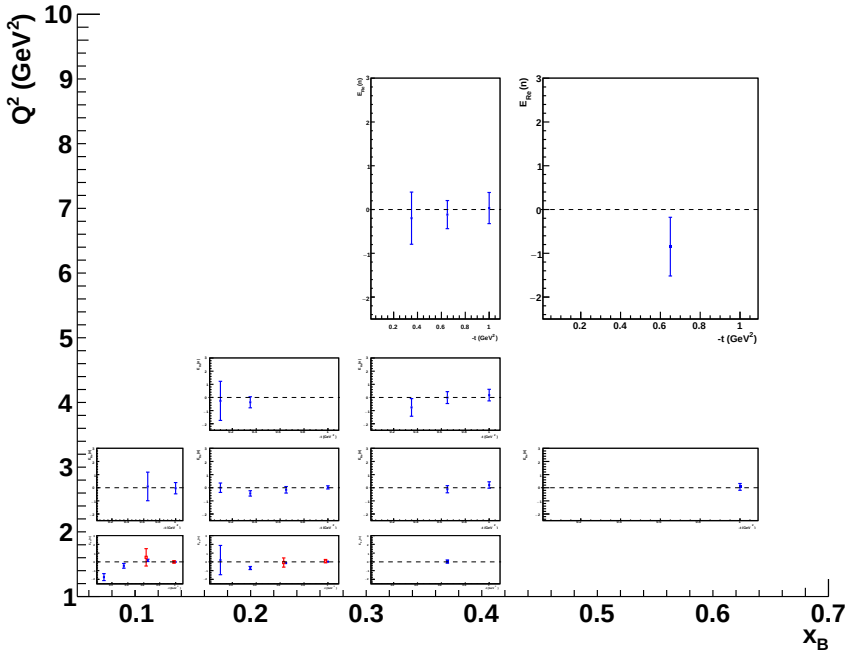

Figure 6. $E_{Re}(n)$ as a function of $-t$, for all bins in Q^2 and x_B. The blue points are the results of the fits including the proposed BCA while the red ones include only already approved experiments.

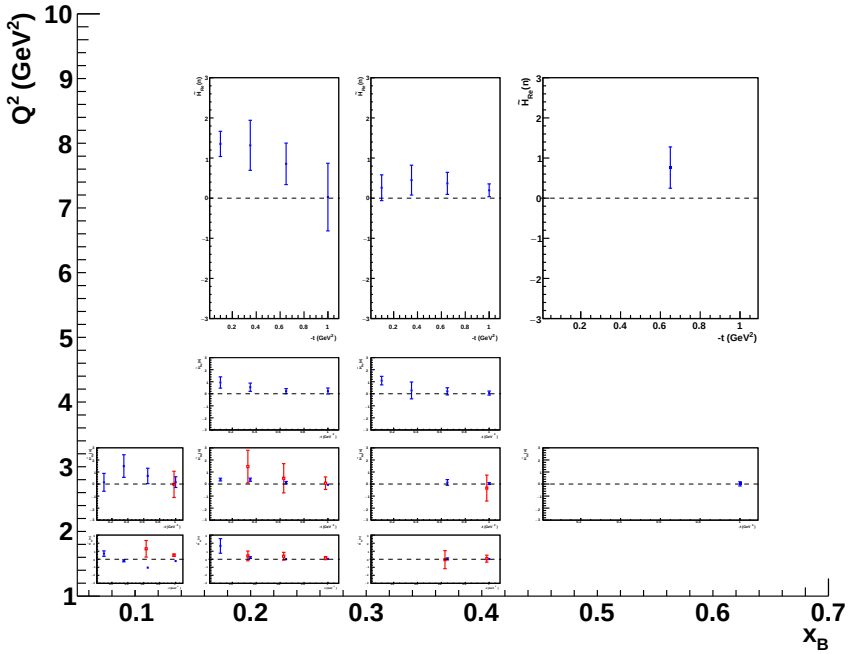

Figure 7. $\widetilde{H_{Re}}(n)$ as a function of $-t$, for all bins in Q^2 and x_B. The blue points are the results of the fits including the proposed BCA while the red ones include only already approved experiments.

terms, such as acceptances, efficiencies, and radiative corrections cancel out

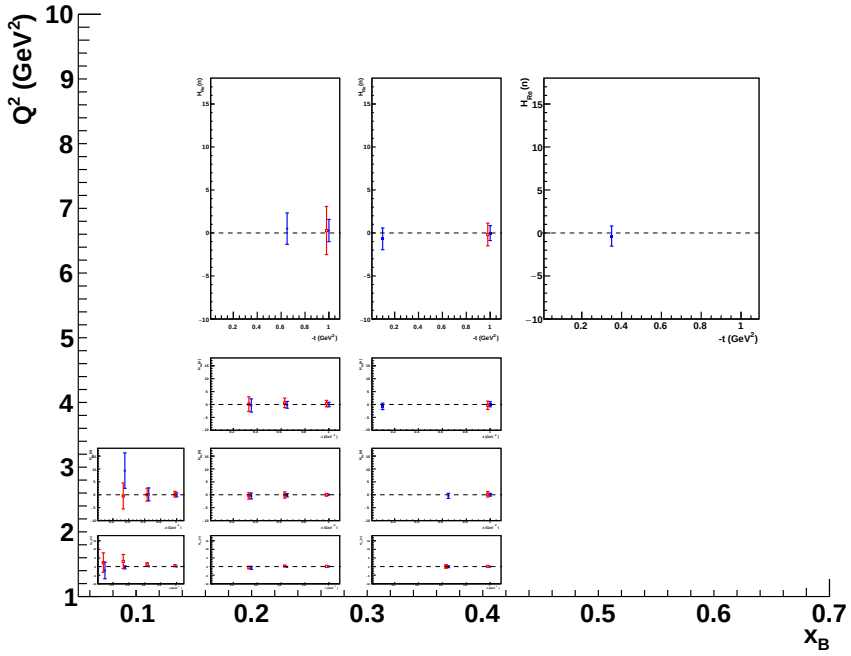

Figure 8. $H_{Re}(n)$ as a function of $-t$, for all bins in Q^2 and x_B. The blue points are the results of the fits including the proposed BCA while the red ones include only already approved experiments.

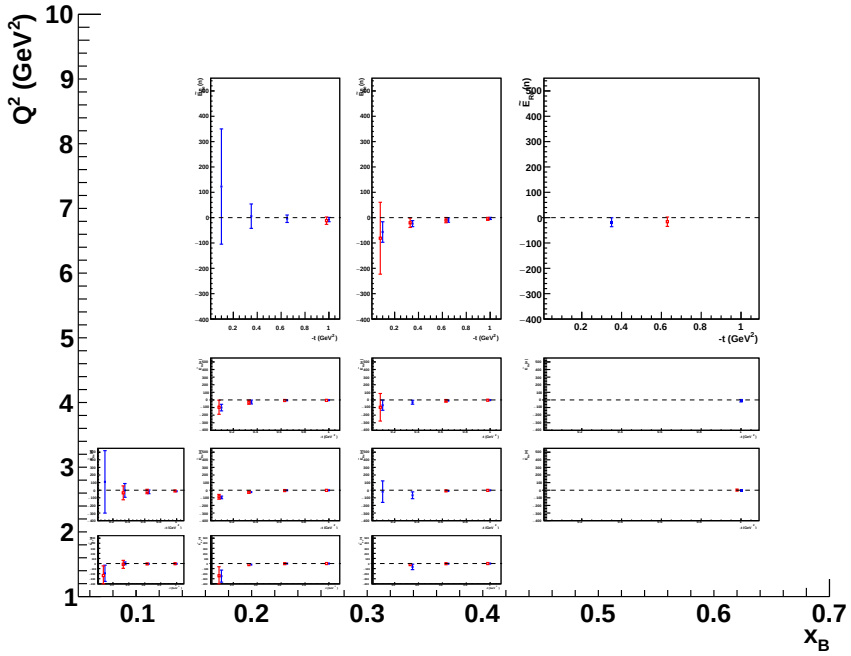

Figure 9. $\widetilde{E_{Re}}(n)$ as a function of $-t$, for all bins in Q^2 and x_B. The blue points are the results of the fits including the proposed BCA while the red ones include only already approved experiments.

at first order. The BCA systematics comprises several contributions (Tab. 1) which are all of roughly the same magnitude. The π^0-background evaluation which depends on the accuracy of the description of the detector acceptance

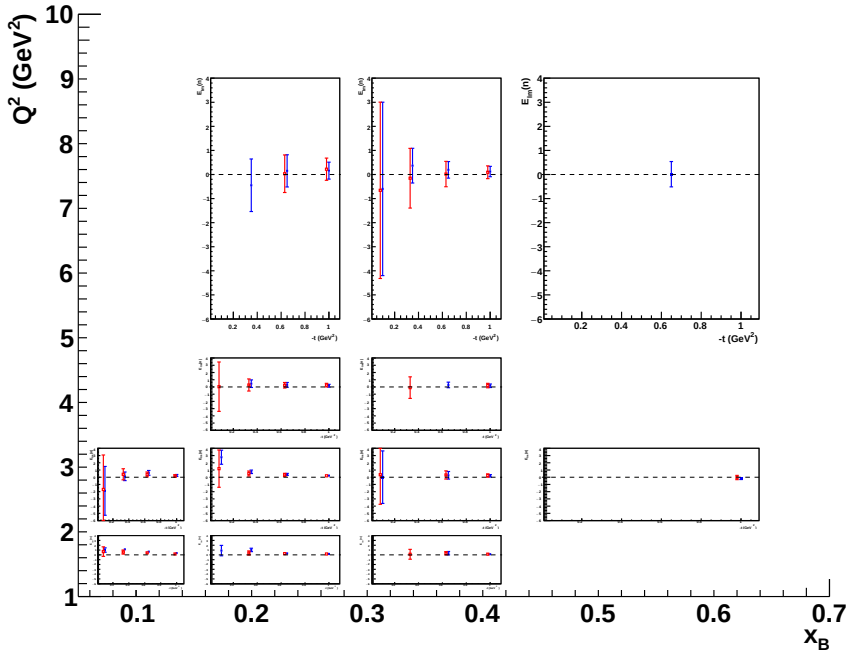

Figure 10. $E_{Im}(n)$ as a function of $-t$, for all bins in Q^2 and x_B. The blue points are the results of the fits including the proposed BCA while the red ones include only already approved experiments.

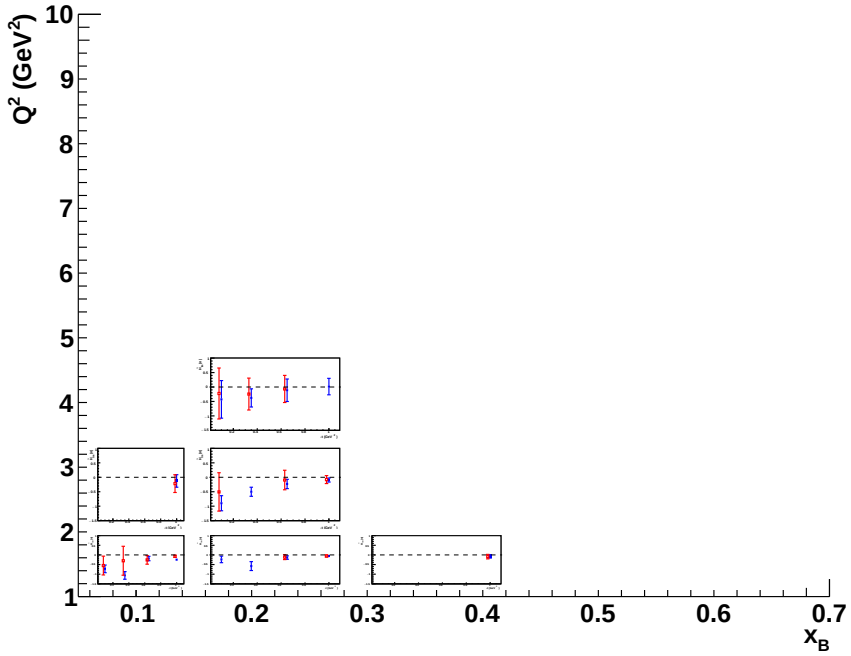

Figure 11. $\widetilde{H_{Im}}(n)$ as a function of $-t$, for all bins in Q^2 and x_B. The blue points are the results of the fits including the proposed BCA while the red ones include only already approved experiments.

and efficiency, will contribute 5% to the overall systematic uncertainties. A similar contribution is expected from n-γ misidentification. Due to its strong variation as a function ϕ, the acceptance will bring an additional 3% system-

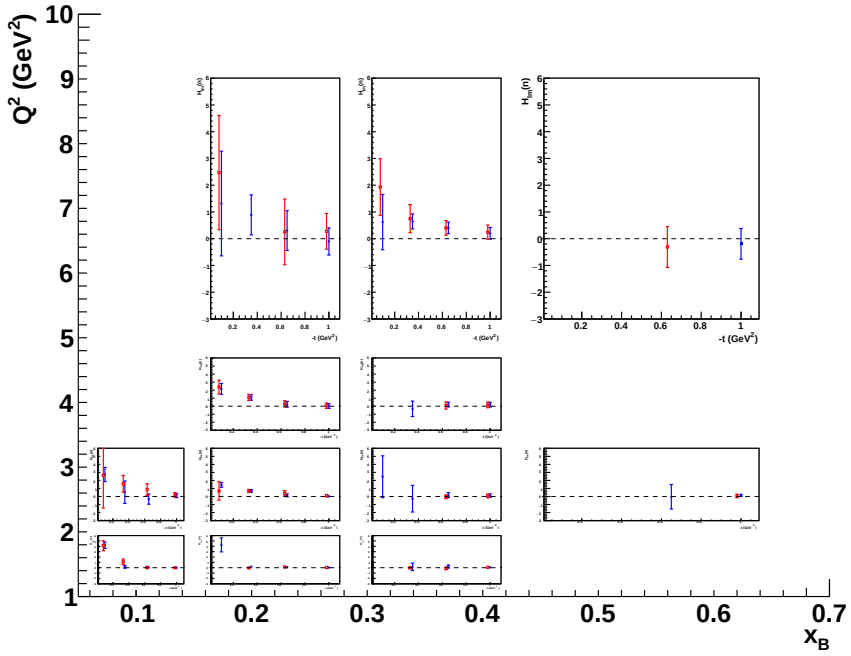

Figure 12. $H_{Im}(n)$ as a function of $-t$, for all bins in Q^2 and x_B. The blue points are the results of the fits including the proposed BCA while the red ones include only already approved experiments.

Source of error	$\sigma(A_C)^{Sys.}$
Beam charge measurement	3%
π^0 contamination	5%
Acceptance	3%
Radiative corrections	3%
n-γ misidentification	5%
Total	9%

Table 1. Expected systematic uncertainties of the proposed measurement.

atic error. A summary of the uncertainties induced by the various sources is reported in Tab. 1. The total systematic uncertainty is expected to be contained within 10% in average.

7.7 Summary

The strong sensitivity to the real part of the GPD E^q of the beam charge asymmetry for DVCS on a neutron target makes the measurement of this observable particularly important for the experimental GPD program of Jefferson Lab. This sensitivity is maximal for values of x_B which are attainable only with a 11 GeV beam. Model predictions show that for possible CLAS12 kinematics, this asymmetry can be comparable in size to the BSA obtained

for p-DVCS.
GEANT4-based simulations show that a total of 80 days of beam time at full luminosity with CLAS12 will allow to collect good statistics for the n-DVCS BCA over a large phase space. The addition of this observable to already planned measurements with CLAS12, will permit the model-independent extraction of the real parts of the $\mathcal{E}_n$ and $\widetilde{\mathcal{H}_n}$ CFF of the neutron over the whole available phase space. Combining all the neutron and the proton CFFs obtained from the fit of n-DVCS and p-DVCS observables to be measured at CLAS12, will ultimately allow the quark-flavor separation of all GPDs.

8 pDVCS-SHMS

Spokesperons:

9 Dark photon search

Searching for Dark Photon with Positrons at Jefferson Lab

Abstract

Spokesperons: M. Battaglieri, A. Celentano, L. Marsicano
(lmarsicano@ge.infn.it)

The Standard Model (SM) of elementary particles and interactions is able to describe with an extraordinary precision ordinary matter in a variety of different environments and energy scales. However, some phenomena such as Dark Matter (DM), neutrino masses and matter-antimatter asymmetry do not fit in the scheme, calling for new physics beyond the SM. DM existence is highly motivated by various astrophisical observations but its fundamental properties remain to date unknown. Experimental efforts have been mainly focused, until today, in the WIMPs search (Weakly Interacting Massive Particles): in this paradigm, DM is made of particles with mass of order of $\sim 100 - 1000$ GeV interacting with the Standard Model via Weak force. Despite attaining the highest energy ever reached at accelerators, LHC has not yet been able to provide evidence for WIMPs-like particles. The same null results in direct detection of halo DM strongly constrains this class of models.

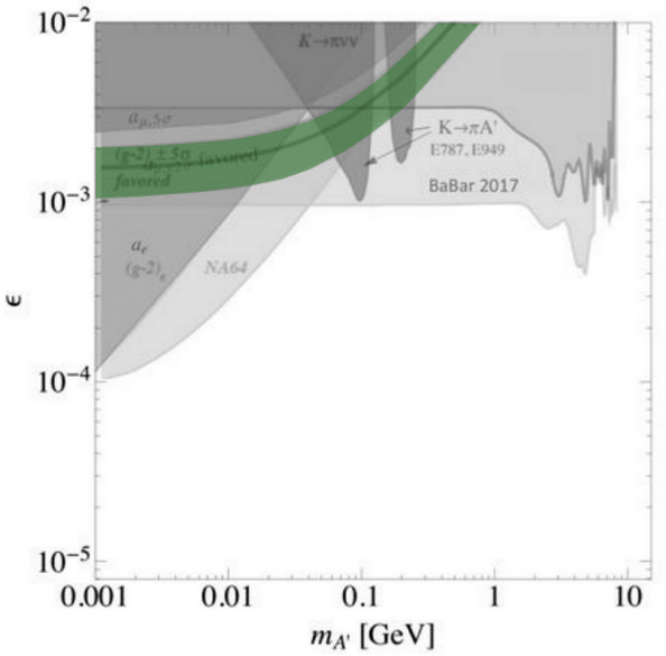

Figure 13. Current exclusion limits for A' invisible decay.

Recently, the interest in new scenarios predicting DM candidates with lower masses has grown. Various models postulate the existence of a hidden sector interacting with the visible world through new *portal* interactions that are constrained by the symmetries of the SM. In particular, DM with mass below 1 GeV/c^2 interacting with the Standard model particles via a light boson (a heavy photon or A', also called dark photon) represents a well motivated scenario that generated many theoretical and phenomenological studies. In this specific scenario the DM, charged under a new gauge symmetry $U(1)_D$ [Hol86], interacts with electromagnetic charged SM particles through the exchange of a dark photon. The interaction between the A' and SM particles is generated effectively by a *kinetic mixing* operator. The low energy effective Lagrangian

extending the SM to include dark photons can thus be written as

$$L_{eff} = L_{SM} - \frac{\epsilon}{2} F^{\mu\nu} F'_{\mu\nu} - \frac{1}{4} F'^{\mu\nu} F'_{\mu\nu} + \frac{1}{2} m^2_{A'} A'_{\mu} A'^{\mu} \tag{41}$$

where $F_{\mu\nu}$ is the usual electromagnetic tensor, $F'_{\mu\nu}$ is the A' field strength, $m_{A'}$ is the mass of the heavy photon, and ϵ is the mixing coupling constant. In this scenario, SM particles acquire a dark *millicharge* proportional to ϵ^2. The value of ϵ can be so small as to preclude the discovery of the A' in the experiments carried out so far.

The decay of the A' depends on the ratio between its mass and the mass of the dark sector particles: if the dark photon mass is smaller than twice the muon mass and no dark sector particle lighter than the A' exists, it can only decay to e^+e^- pairs (*Visible Decay*). If the mass of the A' is higher than twice the mass of the lightest dark matter particle χ, it decays to $\chi\bar{\chi}$ pairs (*Invisible Decay*). In this LOI we address only this last scenario (Fig. 13).

9.2 Annihilation induced A′ production

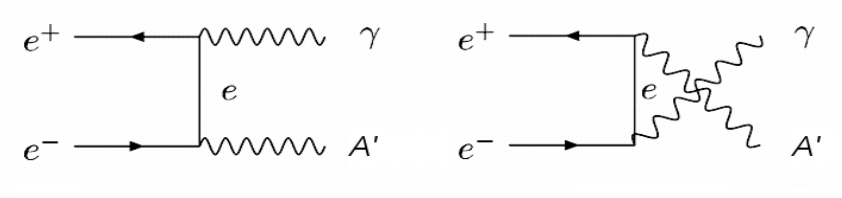

Figure 14. A' production via e^+e^- annihilation.

The A' can be produced in e^+e^- annihilation, via the $e^+e^- \rightarrow \gamma A'$ reaction (Fig. 14). Several experiments have been proposed to search for the production of A' in this process: Dark Light [Fis11], PADME@LNF [Rag14], MMAPS [Ale17], and VEPP-3 [Woj17]. The first e^+ on target experiment searching for A' is PADME (Positron Annihilation into Dark Matter Experiment) which uses the 550 MeV positron beam provided by the DAΦNE linac at LNF (Laboratori Nazionali di Frascati) impinging on a thin diamond target.

The experiment involves the detection of the photons from the annihilation process with a BGO electromagnetic calorimeter placed $\sim$ 2 m downstream of the interaction target. The A' leaves the detector area without interacting. A magnetic field of $\sim$1 T bends away from the calorimenter the positron beam and all the charged particles produced in the target. A single kinematic variable, the missing mass, is computed for each event

$$M^2_{miss} = (P_{e^-} + P_{beam} - P_{\gamma})^2 \tag{42}$$

wich distribution peaks at $M^2_{A'}$ in case of production of the A'. All processes resulting in a single γ hitting the calorimeter constitute the experimentel background: bremsstrahlung, annihilation into 2γ ($e^+e^- \rightarrow \gamma\gamma$), annihilation into 3γ ($e^+e^- \rightarrow \gamma\gamma\gamma$)... In order to reduce the bremsstrahlung background, the

PADME detector features an active veto system composed of plastic scintillators: positrons losing energy via bremmstrahlung in the target are detected in the vetos, allowing to reject the event. However the high bremsstrahlung rate is an issue for this class of experiments, limiting the maximum viable beam current. For this reason, a beam with a continuous structure would be the best option for a PADME-like experiment.

The sensitivity of PADME-like experiments in the A' parameter space is constrained by the available energy in the center of mass frame: with a beam energy of ∼500 MeV, PADME can search for masses up to 22.5 MeV. Higher energy positron beams are required to exceed these limits. In this LOI, the achievable sensitivity of a Dark Photon experiment using the proposed 11 GeV continuous positron beam at JLab is discussed.

9.3 Searching for A' with positrons at Jefferson Lab

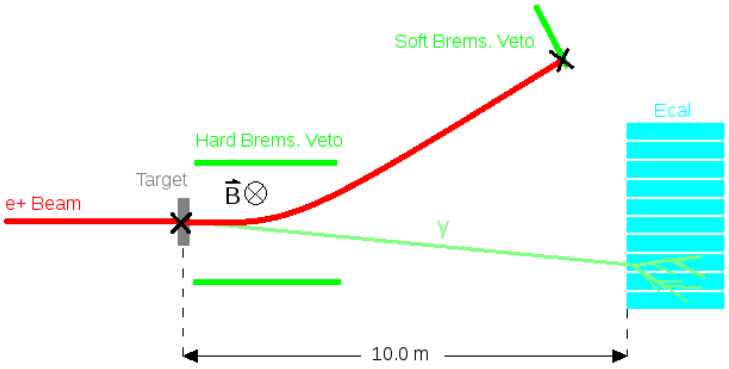

Figure 15. Schematic of the proposed experiment at Jefferson Lab.

The perspective of a high energy continuous positron beam at Jlab is particularly attractive to enlarge the reach of the A' search in the annihilation channel. For a 11 GeV positron beam, the mass region up to ∼106 MeV can be investigated. The experimental setup foreseen for such an experiment at JLab is presented in Fig. 15. It features:

- *i)* A 100 μm thick carbon target, as a good compromise between density and a low Z/A ratio to minimize bremsstrahlung production;
- *ii)* A 50 cm radius highly segmented ($1\times1\times20$ cm^3 crystals) electromagnetic calorimeter placed 10 m downstream of the target, and with the energy resolution $\sigma(E)/E$=$0.02/\sqrt{E(GeV)}$;
- *iii)* An active veto system with a detection efficiency higher than 99.5% for charged particles;
- *iv)* A magnet supporting a field of 1 T over a 2 m region downstream of the target, and bend the positron beam.

Experimental projections are evaluated assuming an adjustable beam current betwen 10-100 nA, a momentum dispersion beeter than 1%, and an angular dispersion better than 0.1 mrad. It should be noticed that momentum and angular dispersion are critical parameters for such an experiment, since a good

knowledge of the beam particles initial state is fundamental for the missing mass calculation.

9.4 Experimental projections

The study of the reconstructed missing mass distribution for the background events serves as a basic criteria to evaluate the sensitivity of the proposed experimental setup. As discussed previously, the main background processes of this experiment are bremsstrahlung and electron-positron annihilation into 2 or 3 photons, which can result in a single hit in the calorimeter. Different strategies were adopted to study the impact of these backgrounds.

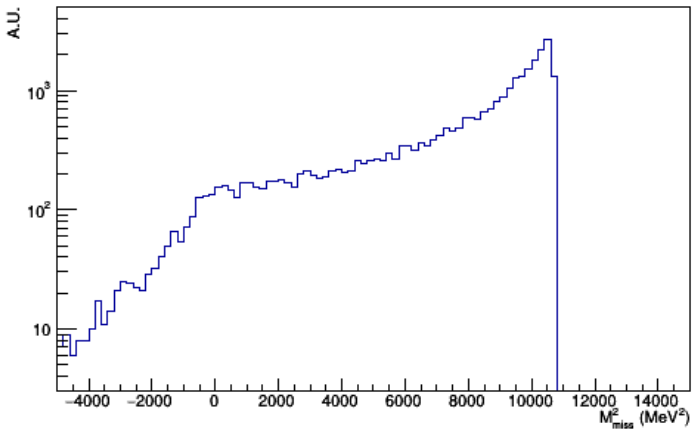

Figure 16. Calculated missing mass spectrum of bremsstrahlung events.

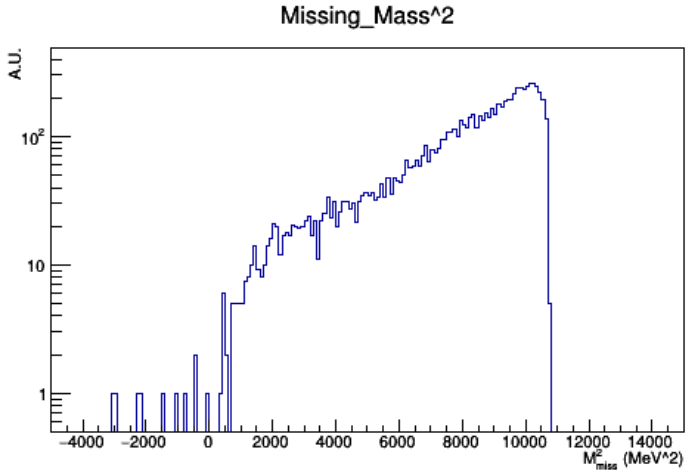

Figure 17. Calculated missing mass spectrum of 3 photons events.

Considering the bremsstrahlung background, a full GEANT4 [Ago03] simulation of the positron beam interacting with the target was performed. The missing mass was computed for all bremsstrahlung photons reaching the calorimeter volume, accounting for the detector angular and momentum resolution.

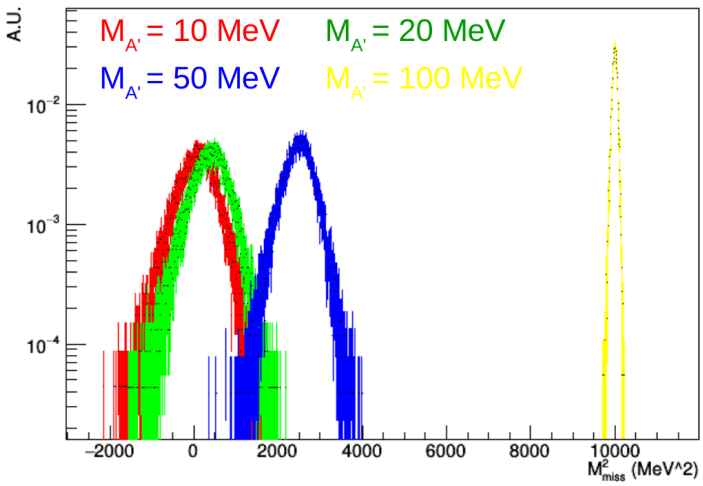

Figure 18. Calculated missing mass spectrum of signal events at 4 different $m_{A'}$ values.

Figure 16 shows the obtained spectrum. The total rate of expected bremsstrahlung events for positron on target was scaled accounting for the effect of the veto system.

The annihiliation into 2 or 3 photons is much less frequent than bremsstrahlung and was therefore studied differently: events were generated directly using CALCHEP [Puk04] which provided also the total cross sections for the processes. As in the case of bremsstrahlung, the missing mass spectrum was computed for events with a single γ-hit in the calorimeter. This study proved that, if an energy cut of 600 MeV is applied, the 2γ-background becomes negligible. This is due to the closed kinematics of the $e^+e^- \to \gamma\gamma$ process: asking for only one photon to hit the detector translates in a strong constraint on its energy. This argument is not valid for the 3γ-events: the number of background events from this process is in fact not negligible (see Fig. 17 for the missing mass spectrum).

Signal events were simulated using CALCHEP. The widths $\sigma(m_{A'})$ of the missing mass distributions of the measured recoil photon from the $e^+e^- \to \gamma A'$ process were computed for six different values of the A' mass in the 1-103 MeV range. Figure 18 shows the corresponding spectra: the missing mass resoluton of the signal is maximum for at high A' masses and degrades at low masses ($m_{A'} < 50$ MeV). As for the annihilation background, CALCHEP provides the total cross section of the process for a full coupling strength. It is then necessary to multiply it with ϵ^2 to obtain the cross section for different coupling values.

The reach of the proposed experiment is obtained from the comparison of the signal and background spectra. A period of 180 days at 10(100) nA positron beam current is considered. $N_s(m_{A'})$ representing the number of expected signal events for a given mass $m_{A'}$ at full coupling, $N_B(m_{A'})$ representing the number of expected total background events within the missing mass in the interval $[m^2_{A'} - 2\sigma(m^2_{A'}); m^2_{A'} + 2\sigma(m^2_{A'})]$, the minimum measurable ϵ^2 coupling

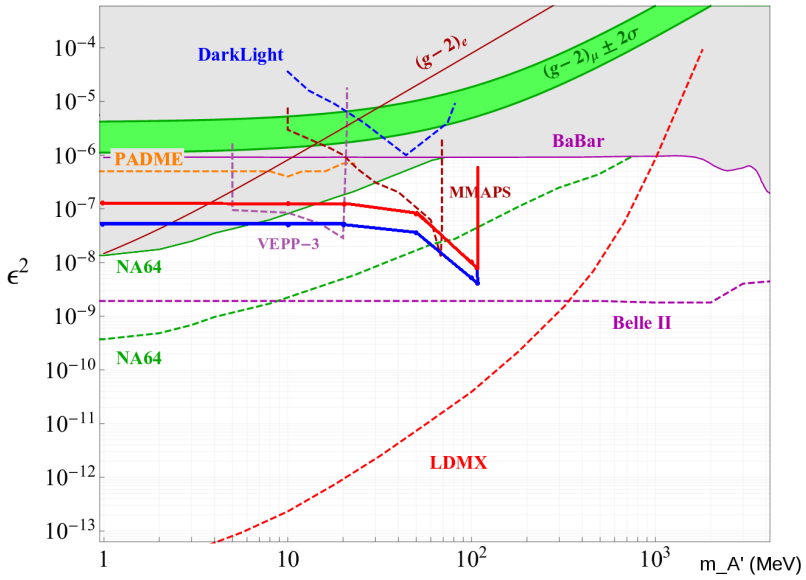

Figure 19. Projected exclusion limits in the A' invisible decay parameter space for a 180 days experiment with a 10 nA (red curve) and 100 nA (blue curve) 11 GeV positron beam at Jefferson Lab.

writes

$$\epsilon^2_{min}(m_{A'}) = 2\frac{\sqrt{N_B(m_{A'})}}{N_S(m_{A'})}\,. \tag{43}$$

Corresponding in the $(m_{A'}, \epsilon^2)$ phase space are shown in Fig. 19. Even at low positron beam current (10 nA), an A'-search experiment at Jefferson Lab will exceed the sensitivity of other current experiments, probing a significant region of the unexplored parameter space.

9.5 Summary

Making use of the future JLab high energy positron beam with a current in the range of tens of nAs, a PADME-like experiment at JLab running over 180 days will extend the A' mass reach up to 100 MeV and will lower the exclusion limit for invisible A' decay by up to a factor of 10 in ϵ^2.

10 Conclusions

References

[Abb16] (PEPPo Collaboration) D. Abbott *et al.* Phys. Rev. Lett. **116** (2016) 214801.

[Add10] P. Adderley *et al.* Phys. Rev. Acc. Beams **13** (2010) 010101.

[Ago03] S. Agostinelli *et al.* Nucl. Inst. Meth. A **506** (2003) 250.

[Akh74] A.I. Akhiezer, M.P. Rekalo, Sov. J. Part. Nucl. **4** (1974) 277.

[Ala09] A. El Aloui and E. Voutier, CLAS Note **2009-024** (2009).

[Ale08] G. Alexander *et al.* Phys. Rev. Lett. **108** (2008) 210801.

[Ale17] J. Alexander, EPJ Web Conf. **142** (2017) 01001.

[And13] (Q_{weak} Collaboration) D. Androić *et al.* Phys. Rev. Lett. **111** (2013) 141803; D. Androić *et al.* Nature **557** (2018) 207.

[Ani06] (HAPPEX Collaboration) K.A. Aniol *et al.* Phys. Rev. Lett. **96** (2006) 022003; K.A. Aniol *et al.* Phys. Lett. B **635** (2006) 275; A. Acha *et al.* Phys. Rev. Lett. **98** (2007) 032301.

[Arn81] R. Arnold, C. Carlson, F. Gross, Phys. Rev. C **23** (1981) 363.

[Arm05] (G0 Collaboration) D.S Amstrong *et al.* Phys. Rev. Lett. **95** (2005) 092001; D. Androić *et al.* Phys. Rev. Lett. **104** (2010) 012001; D. Androić *et al.* Phys. Rev. Lett. **107** (2011) 022501; D. Androić *et al.* Phys. Rev. Lett. **108** (2012) 122002.

[Bat11] M. Battaglieri, R. De Vita, C. Salgado, S. Stepanyan, D. Watts, D. Weygand *et al.* JLab Experiment **E12-11-005** (2011).

[Bel02] A.V. Belitsky, D. Müller, A. Kirchner, Nucl. Phys.B **629** (2002) 323.

[Bel05] A.V. Belitsky, A.V. Radyushkin, Phys. Rep. **418** (2005) 1.

[Bet34] H.A. Bethe, W. Heitler, Proc. Roy. Soc. London A **146** (1934) 83.

[Bro81] S.J. Brodsky, G.P. Lepage, Phys. Rev. D **22** (1981) 2157.

[Die03] M. Diehl, Phys. Rep. **388** (2003) 41.

[Die09] M. Diehl, *Cont. to the CLAS12 European Workshop* (Genova (Italy), 2009).

[Fis11] R. Fisher, R. Milner *et al.* JLab Experiment **E12-11-008** (2011).

[Gay02] (Hall A Collaboration) O. Gayou *et al.* Phys. Rev. Lett. **88** (2002) 092301.

[Goe01] K. Goeke, M.V. Polyakov, M.Vanderhaeghen, Prog. Part. Nucl. Phys. **47** (2001) 401.

[Gui03] P.A.M. Guichon and M. Vanderhaeghen, Phys. Rev. Lett. **91** (2003) 142303.

[Gui05] M. Guidal, M.V. Polyakov, A.V. Radyushkin, M. Vanderhaeghen, Phys. Rev. D **72** (2005) 054013.

[Gui08] M. Guidal, Eur. Phys. J. A **37** (2008) 319.

[Gui13] M. Guidal, H. Moutarde, M. Vanderhaeghen, Rep. Prog. Phys. **76** (2013) 066202.

[Hol86] B. Holdom, Phys. Lett. B **166** (1986) 186.

[Hos16] N. d'Hose, S. Niccolai, A. Rostomyan, Eur. Phys. J. A **52** (2016) 151.

[Ji97] X. Ji, Phys. Rev. Lett. **78** (1997) 610.

[Jon00] (Hall A Collaboration) M.K. Jones *et al.* Phys. Rev. Lett. **84** (2000) 1398.

[Lac80] M. Lacombe *et al.* Phys. Rev C **21** (1980) 861.

[Maz07] M. Mazouz *et al.* Phys. Rev. Lett. **99** (2007) 242501.

[Mul94] D. Müller, D. Robaschick, B. Geyer, F.M. Dittes, J. Hořejši, Fortschr. Phys. **42** (1994) 101.

[Nic11] S. Niccolai, V. Kubarovsky, S. Pisano, D. Sokhan *et al.* JLab Experiment **E12-11-003** (2011).
[Nic15] S. Niccolai, A. Biselli, C. Keith, S. Kuhn, S. Pisano, D. Sokhan *et al.* JLab Experiment **C12-15-004** (2015).
[Omo06] T. Omori et al., Phys. Rev. Lett. **96** (2006) 114801.
[Puc10] (Hall A Collaboration) A.J.R. Puckett *et al.* Phys. Rev. Lett. **104** (2010) 242301.
[Puk04] A. Pukhov, (2004) arXiv:0412191.
[Pun15] V. Punjabi, C.F. Perdrisat, M.K. Jones, E.J. Brash and C.E. Carlson, Eur. Phys. J. A **51** (2015) 79.
[Rad97] A.V. Radyushkin, Phys. Rev. **D 56** (1997) 5524.
[Rag14] M. Raggi, V. Kozhuharov, Adv. High Energy Phys.**2014** (2014) 959802; arXiv:1403.3041.
[Rek04] M.P. Rekalo, E. Tomasi-Gustafsson, Nucl. Phys. A **742** (2004) 322.
[Ros50] M.N. Rosenbluth, Phys. Rev. **79** (1950) 615.
[Sok64] A.A. Sokolov and I.M. Ternov, Sov. Phys. Dokl. **8** (1964) 1203.
[Ste01] (CLAS Collaboration) S. Stepanyan *et al.* Phys. Rev. Lett. **87** (2001) 182002.
[Van99] M. Vanderhaeghen, P.A.M. Guichon, M. Guidal, Phys. Rev. D **60** (1999) 094017.
[Vou14] E. Voutier, Nuclear Theory **33** (Heron Press, Sofia) (2014) 142; arXiv:1412.1249.
[Woj17] B. Wojtsekhowski *et al.* (2017) arXiv:1708.07901.
[You06] R.D. Young, J. Roche, R.D. Carlini, A.W. Thomas, Phys. Rev. Lett. **97** (2006) 102002.